Supporting Information

Addressing the Stability Gap in Photoelectrochemistry: Molybdenum Disulfide Protective Catalysts for Tandem III-V Unassisted Solar Water Splitting

*Micha Ben-Naim[†1], Reuben J. Britto[†1], Chase W. Aldridge[2], Rachel Mow[2], Myles A. Steiner[3], Adam C. Nielander[1], Laurie A. King[1,4], Daniel J. Friedman[3], Todd G. Deutsch[2], James L. Young[2], Thomas F. Jaramillo[1]**

[1]Department of Chemical Engineering, Shriram Center, Stanford University, 443 Via Ortega, Stanford, California 94305, United States

[2]Chemistry and Nanoscience Center, and Materials Science Center, National Renewable Energy Laboratory, Golden, Colorado 80401, United States

[3]National Center for Photovoltaics, National Renewable Energy Laboratory, Golden, Colorado 80401, United States

[4]Faculty of Science and Engineering, Manchester Metropolitan University, Manchester M1 5GD, U.K.

[†]These authors contributed equally to this work

Corresponding Author:

*Thomas F. Jaramillo. Email: jaramillo@stanford.edu

1. Experimental Methods

III-V Fabrication

Semiconductor structures were grown by atmospheric pressure metalorganic vapor phase epitaxy (MOVPE) on a custom-built reactor. The source gases for the semiconductors included trimethylgallium, triethylgallium, trimethylindium, trimethylaluminum, arsine and phosphine; hydrogen selenide and disilane were the sources for selenium and silicon n-type dopants; diethylzinc and carbon tetrachloride were the sources for the zinc and carbon p-type dopants. Nitrogen was included in a GaInAsN front contact layer for photovoltaic test structures, and was sourced from dimethylhydrazine. All sources were transported to the reactor in a 6 lpm flow of purified hydrogen carrier gas.

The structures were grown on 350 µm thick (001) GaAs:Si substrates, miscut 6° toward the <111>A direction. Prior to growth, the substrate was cleaved to a 20 mm x 30 mm rectangle and etched for 2 minutes in (2:1:10) $NH_4OH:H_2O_2:H_2O$ followed by a rinse in de-ionized water. The inverted growth proceeded from a $GaInP_2$ stop-etch layer at 700 °C, followed by a GaInAsN/GaAs front contact layer at 570 °C, then the GaInAsP top cell grown at 650 °C and ~3.6 µm h^{-1}, an $Al_{0.3}Ga_{0.7}As$/GaAs tunnel junction interconnect grown at 600 °C and 2-3 µm h^{-1}, the GaAs bottom cell grown at 650 °C and ~5.8 µm h^{-1}, and finally the $Al_{0.3}Ga_{0.7}As$ back contact layer at 620 °C and ~2.1 µm h^{-1}. The structure is indicated in Table S1. Growth rates and compositions are nominal but are based on regular calibrations of the reactor. All layers were grown with a V/III ratio >10 and as high as 500, as is typical for MOVPE. The structure was cooled down to room temperature under an arsine overpressure. The top cell included an $Al_{0.27}Ga_{0.25}In_{0.48}P$ rear minority-carrier confinement layer. The bottom cell included $GaInP_2$ front and rear minority-carrier confinement layers. Several calibration growths were necessary to tune the composition of

the GaInAsP top cell, to simultaneously achieve a lattice-matched alloy with a bandgap of ~1.68 eV, as determined by quantum efficiency measurements on single junction cells. For the calibration samples, lattice-matching was determined by an *in-situ* measurement of the stress as derived from the wafer curvature,[1] and an *ex-situ* x-ray diffraction measurement of an (004) rocking curve. The bandgap of the quaternary was evaluated by room-temperature photoluminescence. Additional details can be found in refs 2 and 3.

After the inverted growth, a gold back contact was electroplated to the $Al_{0.3}Ga_{0.7}As$ back contact layer. The semiconductor was bonded with a low viscosity epoxy to a silicon mechanical handle, the GaAs substrate was etched away with NH_4OH:H_2O_2 (~1:2 by volume), and the $GaInP_2$ and GaInAsN/GaAs layers were etched away with appropriate etchants. After deposition of the catalyst, Shipley S1818 photoresist was used to define a mesa area and individual devices were isolated by standard wet-chemical etching through the semiconductor layers, down to the electroplated back contact.

Table S1. Layer structure of the III-V device, including nominal thickness and carrier concentration.

Layer	Thickness (nm)	Doping	Approx. Carrier Concentration (cm^{-3})
GaInAsP	25	n	$2\text{-}4 * 10^{18}$
GaInAsP	2000	p	$<1 * 10^{17}$
$Al_{0.27}Ga_{0.25}In_{0.48}P$	200	p	$\sim1 * 10^{18}$
GaInP	10	p	$\sim1 * 10^{18}$
$Al_{0.3}Ga_{0.7}As$	20	p	$>1 * 10^{19}$
GaAs	12	n	$>1 * 10^{19}$
$Al_{0.3}Ga_{0.7}As$	50	n	$\sim3 * 10^{18}$
GaInP	30	n	$\sim3 * 10^{18}$
GaAs	85	n	$\sim1\text{-}2 * 10^{18}$
GaAs	2000	p	$\sim1 * 10^{17}$
GaInP	300	p	$\sim1\text{-}2 * 10^{18}$
$Al_{0.3}Ga_{0.7}As$	200	p	$>2 * 10^{19}$
Gold	> 1000		

MoS_2 Deposition

An MoS_2 coating has previously been shown to stabilize a $GaInP_2$ top surface, providing motivation for pairing MoS_2 with this tandem absorber architecture.[4] The portion of the wafer to be coated with MoS_2 was diced and Mesa etched.[5] A shadow mask consisting of Kapton tape with a circular hole 1 cm in diameter was placed over the device before it was transferred to a DC magnetron sputter coater. A thin layer of Mo metal was deposited onto the wafer at a rate of 7.2 nm min^{-1} for 30 seconds to achieve a nominal thickness of 3.6 nm. Immediately after Mo deposition, the wafer was transferred to a tube furnace (Mellen 1 zone) and sulfidized in 90% H_2/10% H_2S held at 150 °C for 1 h to create the MoS_2 layer. The Kapton shadow mask was then removed, and the device was made into an electrode by covering undeposited areas with epoxy (Loctite E-120HP).

PtRu Deposition

The PtRu was deposited via flash sputtering in which the sample was exposed briefly (~2 s duration) by a rapid pneumatic shutter actuation to achieve very low PtRu loading ~500 ng cm^{-2}.[5] Following the sputtering, the device was Mesa etched and then epoxied into an electrode.

Electrochemical Characterization

Electrodes were tested in a two-compartment cell using 0.5 M sulfuric acid (OmniTrace® EMD Millipore) electrolyte with 1 mM Triton X-100 surfactant added to facilitate H_2 bubble detachment by reducing surface tension.[6] The counter electrode consisted of a RuO_2 powder compressed into a Pt mesh. The two compartments were separated by a proton-conducting Nafion® membrane. Three-electrode measurements were conducted with a $Hg/HgSO_4$ reference electrode

(0.5 M H_2SO_4), and two-electrode measurements used the RuO_2 counter electrode. All LSVs were measured with a scan rate of 20 mV/s, starting at negative potentials and sweeping until the current density reached a value above –0.5 mA cm^{-2}. The working electrodes were illuminated by a 250 W quartz tungsten-halogen lamp with a water-filled IR filter and light shaping diffuser (Newport), and illumination intensity was set to ~1.3-sun using a $GaInP_2$ (1.8 eV) reference cell calibrated to the AM1.5G standard.[7] Optical characterization was collected with an in situ stereomicroscope (AM7915MZTL – EDGE, Dino-Lite).

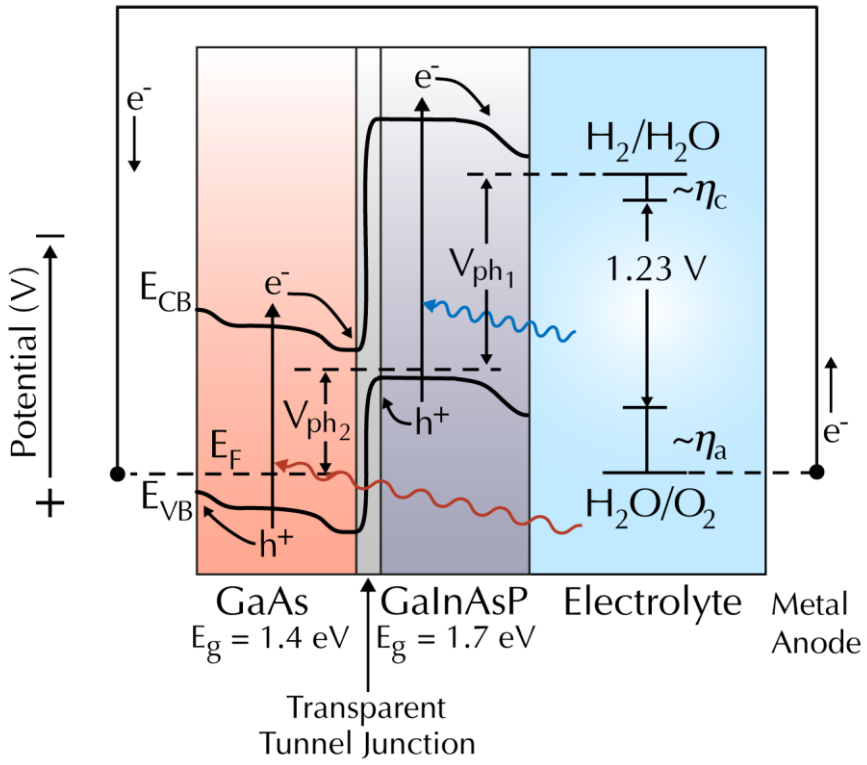

Figure S1. Band diagram schematic for GaInAsP/GaAs tandem devices showing light absorption in the GaInAsP and GaAs semiconductors generating electron-hole pairs. Holes generated in the GaAs bottom cell are collected in the gold back contact and flow through an external wire to the counter electrode anode (RuO_x) to facilitate oxygen evolution. Electrons generated in the GaInAsP top cell are driven to the catalyst layer on the surface to evolve H_2.

2. Additional Electrochemical Characterization

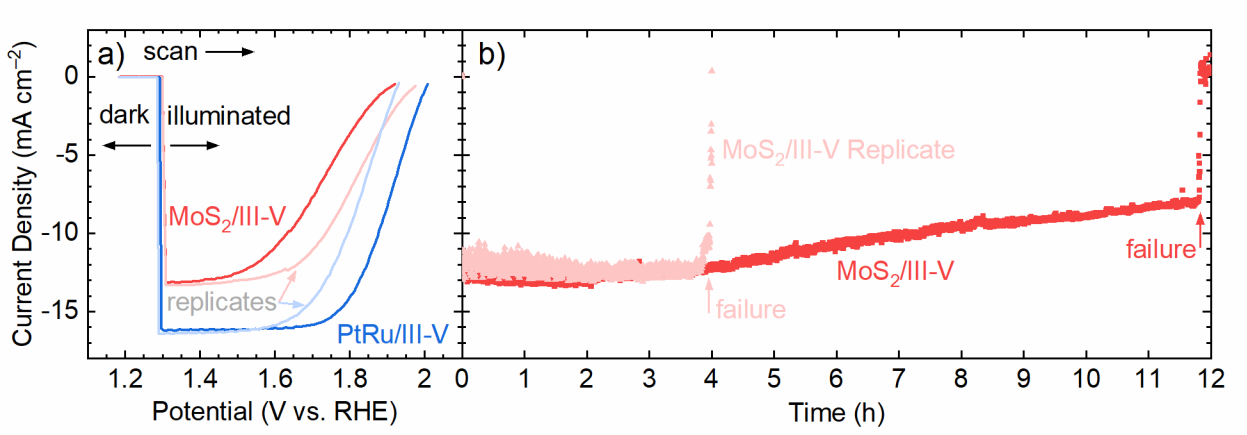

Figure S2. Electrochemical characterization of the MoS_2/III-V and PtRu/III-V unassisted water splitting devices with replicates prepared in the same batch . a). Three-electrode LSVs measured with a $Hg/HgSO_4$ reference electrode and RuO_2 counter electrode. Scans were collected starting from more negative potential and sweeping to more positive potentials with a scan rate of 20 mV s^{-1}. The first 100 mV of the scan was measured with light excluded, while the remainder of the scan was conducted under 1.3-sun illumination. The scan was stopped when the current density reached –0.5 mA cm^{-2}. Two samples for each of the MoS_2/III-V and PtRu/III-V devices were tested with the replicate data shown in the light red and light blue, respectively. b). Two electrode CA measurement taken at short circuit (E = 0 V vs. RuO_2) until device failure for the MoS_2/III-V device shown in the main text (dark red squares) and a replicate device (light red triangles). The replicate device lasted 4.0 h until failure while the first MoS_2/III-V sample lasted 11.8, both of which lasted longer than the PtRu/III-V device.

3. Lamp Spectrum and Solar-to-Hydrogen-Efficiency

The lamp used for all PEC measurements in this work was a 250 W quartz tungsten-halogen lamp with a water-filled IR filter and light shaping diffuser. The illumination intensity was set to ~1.3-sun with a $GaInP_2$ reference cell (1.8 eV) calibrated to the AM1.5G solar spectrum standard such that the current produced by the reference cell equals 1.3 times that under the AM1.5G spectrum. The total irradiance produced by the tungsten lamp with this calibration is 119 mW cm^{-2} (overall, approx. 1.2 suns) We note that there is a significant spectral mismatch between the tungsten lamp and AM1.5G spectra, where there are significantly more photons with E < 1.8 eV in the tungsten lamp spectrum than in the solar spectrum (Figure S3).[8] Thus, this calibration of the tungsten lamp will lead to >1.3 suns worth of photons available for both the top cell (1.7 eV) and bottom cell (1.4 eV) (Table S2).[8] In a tandem absorber system, the overall device current is determined by the smaller of the two currents generated in each junction.[8] Based on the bandgaps of this tandem system, under AM1.5G illumination (1-sun), the bottom cell would have only 9.4 mA cm^{-2} worth of photons available to absorb, while the top cell would have 22.4 mA cm^{-2} (Table S2). However, this tungsten lamp setup outputs 30.8 and 24.3 mA cm^{-2} worth of photons for the top and bottom junctions, respectively, which would lead to significantly inflated photocurrent values compared to a total power measurement with respect to the true AM1.5G spectrum. Thus, this tungsten lamp provides more than double the available photons to the limiting bottom junction compared to the solar spectrum (24.3 mA cm^{-2} vs. 9.4 mA cm^{-2}), even though the overall power output is 1.2 suns. This is why it is so important for STH calculations to take into consideration the laboratory lamp's spectral shape, not just its overall power.

The STH efficiency (η_{STH}) is calculated by equation S1, where j_{SC} is the current density with no applied bias, E^0 is the thermodynamic potential of water splitting at 25 °C (1.23 V), η_F is the faradaic efficiency, and P_{in} is the incoming irradiance power density.[8,9]

$$\eta_{STH} = \frac{j_{SC} \times E^0 \times \eta_F}{P_{in}} \quad \text{(S1)}$$

Past results involving photocathodes coated with a similar MoS_2 coating as in the MoS_2/III-V device[10] and tandem III-V structures with the same PtRu catalyst layer as in the PtRu/III-V device[5] have both been shown to have a η_F of 1, so η_F is assumed to be near unity in this study. In addition, a lower bound for η_F can be calculated by comparing the total charge passed to the total amount of current that could contribute towards non-faradaic processes like corrosion. For both the MoS_2/III-V and PtRu/III-V devices, there is substantial current being generated until their respective sudden failure times. The continued generation of current and appearance of bubbles throughout the CA measurement suggests that both the top and bottom cells must be intact. The total amount of charge that would be required to dissolve the entirety of the 2 μm GaInAsP top cell can be estimated and treated as an upper bound for corrosion current. Cathodic corrosion would release 3 electrons per Ga or In atom,[11] or 12 electrons per unit cell. GaInAsP has a lattice constant of a = 5.65 Å,[12] so dissolution of the entire 2 μm GaInAsP would require 2.13 C cm^{-2}. The MoS_2/III-V and PtRu/III-V devices produced 425 and 119 C cm^{-2}, respectively, so the lower bounds for the η_F are ~ 0.995 and 0.982, respectively.

Because of the excess photons available for absorption by both junctions, using the actual incident power (119 mW cm^{-2}) would give an inflated value for η_{STH}.[8] Using these 1.2-suns as P_{in} would give $\eta_{STH} \approx$ 13% and 16% for the MoS_2/III-V and PtRu/III-V devices, respectively. These values are greater than the calculated theoretical maximum efficiency of 12% for this system, which is not physically reasonable.[5] Thus, when estimating η_{STH}, the value for P_{in} was taken to be

the power of 1-sun irradiance (100 mW cm^{-2}) scaled by the number of suns (by photons) reaching the current-limiting bottom cell (2.58), or $P_{in} \approx 258$ mW cm^{-2}. In other words, illuminating these samples under solar irradiance concentrated to 2.58 suns would be expected to give similar photocurrent to those measured here with the tungsten lamp setup. While this estimation for η_{STH} is not fully representative of the true efficiency under solar illumination, this conservative estimation allows for more accurate comparisons with other reports. Thus, the MoS_2/III-V device demonstrated $\eta_{STH} \approx 6.1\%$ ($j_{SC} = -12.8$ mA cm^{-2}), while the PtRu/III-V sample exhibited $\eta_{STH} \approx 7.6\%$ ($j_{SC} = -16.0$ mA cm^{-2}). The calculated maximum η_{STH} for a 1.7/1.4 eV tandem PEC cell is 12%, so these estimated η_{STH} values are reasonable and physical.[5] While the incident solar power is >1 sun by both the total power and the incident photon flux absorbable by both junctions, it is still in the regime where the photocurrent is expected to be proportional to the incident power due to the low series resistance and relatively low current densities being passed, and thus η_{STH} should not depend on the scaling of the incident spectrum.[13,14]

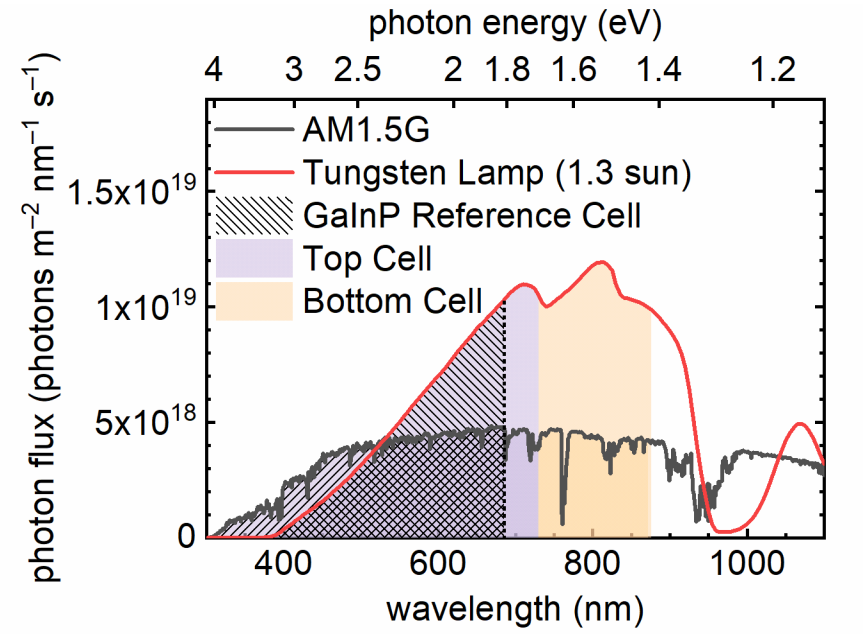

Figure S3. Tungsten lamp photon flux spectrum compared to AM1.5G 1-sun spectrum. The shaded areas in purple and orange represent the total photon flux with energy > 1.7 eV and between 1.4 – 1.7 eV, respectively, which are available for absorption by the top and bottom cell. The tungsten lamp is calibrated to 1.3-sun with a $GaInP_2$ reference diode (1.8 eV, marked by the dotted line).

Table S2. Integrated Photon flux in various energy ranges for the AM1.5G solar spectrum and tungsten lamp spectrum used in the measurements in this study.

Spectrum	Cell	Photon Range	Irradiance (W m^{-2})	Photon flux (n photon m^{-2} s^{-1})	J (mA cm^{-2})	
AM1.5G	1.8 eV Calibration	E > 1.8 eV	457	$1.21 * 10^{21}$	19.3	
	top cell	E > 1.7 eV	511	$1.40 * 10^{21}$	22.4	
	bottom cell	1.7 > E > 1.4 eV	146	$0.59 * 10^{21}$	9.4	
	top + bottom	E > 1.4 eV	658	$1.99 * 10^{21}$	31.8	
Spectrum	Cell	Photon Range	Irradiance (W m^{-2})	Photon flux (n photon m^{-2} s^{-1})	J (mA cm^{-2})	n Suns
Tungsten lamp, scaled to 1.3-sun	1.8 eV Calibration	E > 1.8 eV	490	$1.44 * 10^{21}$	23.1	1.19
	top cell	E > 1.7 eV	625	$1.93 * 10^{21}$	30.8	1.37
	bottom cell	1.7 > E > 1.4 eV	390	$1.52 * 10^{21}$	**24.3**	**2.58**
	top + bottom	E > 1.4 eV	1002	$3.44 * 10^{21}$	55.1	1.73

4. Current-Limiting Junction

Integrated quantum efficiency data for photovoltaic test structures was used to test whether the top or bottom cell would limit the overall device current (Figure S4). External quantum efficiency (EQE), or the number of electrons collected per photon as a function of wavelength, was measured for a single junction GaInAsP cell and a GaAs bottom cell in a tandem GaInAsP/GaAs cell.[3,5] The EQE for these two cells was integrated over the AM1.5G spectrum with no absorption losses and scaled to give a limiting current of 12.8 mA cm^{-2}, matching that of the MoS_2/III-V device. The integrated currents for the top and bottom cells are 21.9 mA cm^{-2} and 12.8 mA cm^{-2}, indicating that the bottom cell would be current-limiting under solar illumination. A similar calculation was performed with the tungsten lamp spectrum taking into account absorption in the MoS_2 and quartz cell and scaled to give the same current of 12.8 mA cm^{-2}.[10] The photocurrents for the top and bottom cell are expected to be 15.4 and 12.8 mA cm^{-2}, so the bottom cell is still current-limiting in the measurements presented here. Under both the solar spectrum and the tungsten lamp used here, the bottom cell would be limiting the overall device current, so the top cell potential will be pinned at open circuit potential. Thus, the durability of the III-V devices under the tungsten halogen lamp will have similar carrier dynamics and stability constraints as under solar irradiance.

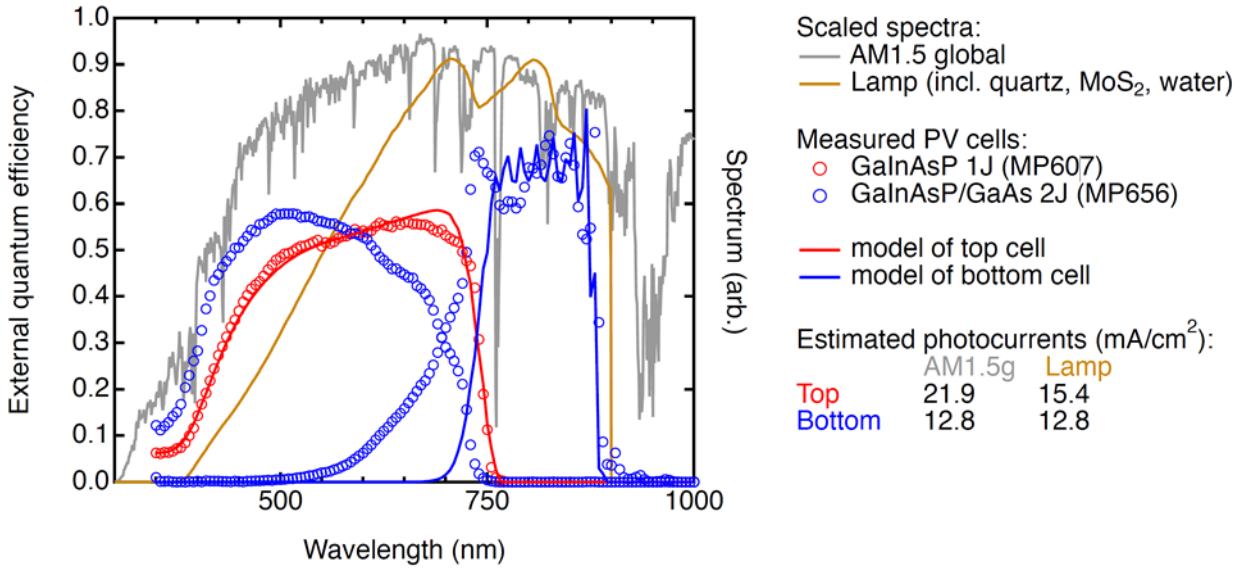

Figure S4. Estimated spectral response for the tandem PEC device. The external quantum efficiencies are shown for test structures. The red data (MP607) is a single junction GaInAsP cell with the same structure as the top cell in our device. The blue data is for a GaInAsP/GaAs tandem. The solid lines show models of the EQE using available optical data for the various layers. The grey and orange lines show the AM1.5-global and tungsten lamp spectra, each scaled so that the integral of the bottom cell EQE over the spectrum yields a photocurrent of 12.8 mA cm^{-2} as measured experimentally. The table on the right shows the tandem to be bottom-limited under both spectra. Note that discrepancies between the model and the data lead to errors that are significantly smaller than the differences in the top and bottom photocurrents, in both cases.

5. Description of Supplemental Movies

Supplemental Movie 1 is a time lapse of the III-V/MoS_2 device surface during the chronoamperometry measurement, starting at 5.7 h of testing and running until 19 h, after device failure at 11.8 h. A frame was taken every 5 min, and the movie has 1 frame per 1 s.

Supplemental Movie 2 is a time lapse of the III-V/PtRu device surface during the chronoamperometry measurement, starting at 0 h of testing and running until 2.25 h, concurrent with device failure. A frame was taken every 1 min, and the movie has 1 frame per 4 s.

6. Comparison of Unassisted Solar Water Splitting Devices with > 1% STH Efficiency

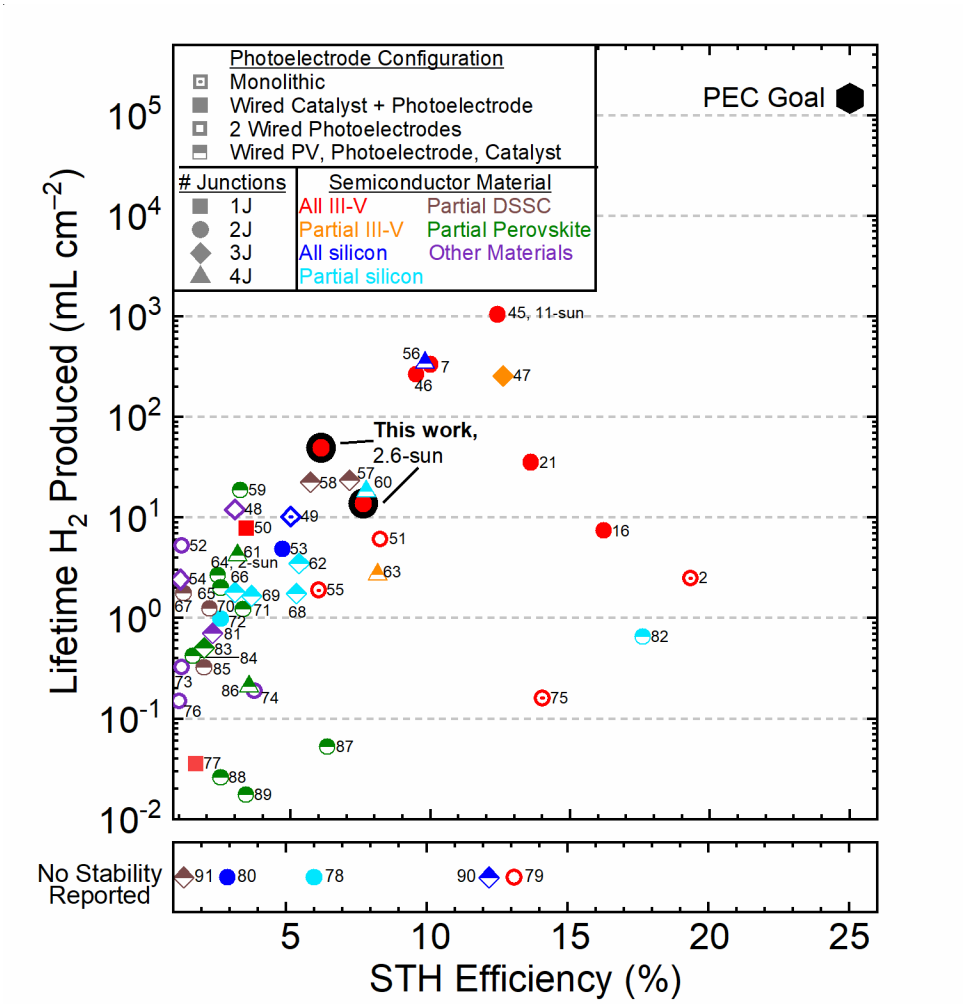

Figure S5. Comparison of solar to hydrogen (STH) efficiency and lifetime H_2 produced for high efficiency (>1% STH) unassisted water splitting devices with at least one photoelectrode integrating a catalyst and semiconductor(s). This plot includes all data in Figure 4 as well as systems that produced <1 mL cm^{-2} H_2, including devices with no reported stability.[15-34] Tabulated data are found in Tables 1 and 2 for systems that produced > 1 mL cm^{-2} H_2 and in Tables S3 and S4 for systems with no reported stability or <1 mL cm^{-2}. Datapoint labels refer to the main text reference #.

Table S3. Tabulated data of unassisted water splitting devices with >1% initial STH which produced <1 mL cm^{-2} lifetime H_2. Architectures consist of photoelectrodes and/or catalysts without a separate, wired photovoltaic. Semiconductor materials are shown in black, catalysts are in red, and protecting/contact layers are in blue

(Photo)cathode	(Photo)anode	Configuration	Initial STH (%)	Stability (h)	Average *J* (mA cm^{-2})	Charge Passed (C)	H_2 Produced (mL cm^{-2})	First Author	Year	Ref #
Ni/Si	FeOOH/$BiVO_4$	Two wired photoelectrodes	2.5	2	1.2	8.5	0.99	Ding	2014	72
Pt/TiO_2/CdS /CGIZS	$CoFeO_x$/$BiVO_4$	Two wired photoelectrodes	1.1	1.2	0.65	2.8	0.33	Hayashi	2018	73
Pt/CdS/CIGS	NiOOH/FeOOH/$BiVO_4$	Two wired photoelectrodes	3.7	0.17	2.7	1.6	0.19	Kobayashi	2018	74
Rh/$GaInP_2$/GaInAs	RuO_2	Monolithic	14	0.033	11.5	1.4	0.16	May	2015	75
Pt/TiO_2/Al_2O_3/CdS/CIGS	NiOOH/FeOOH/$BiVO_4$	Two wired photoelectrodes	1.0	0.5	0.72	1.3	0.15	Chen	2018	76
Pt	$GaSb_xP_{(1-x)}$	Wired catalyst	1.6	0.06	1.4	0.3	0.04	Martinez-Garcia	2018	77
Pt	Au NP/Fe_2O_3/Si	Wired catalyst	6.0	0.67	--			Wang	2014	78
Pt/Ti/pn-GaAs	IrO_x/Ti/np-GaAs	Two wired photoelectrodes	13.1	--				Kang	2017	79
Pt/pin-Si/pin-Si	RuO_2	Wired catalyst	2.9	--				Sakai	1988	80

Table S4. Tabulated data of unassisted water splitting devices with >1% STH which produced <1 mL cm^{-2} lifetime H_2. Architectures consist of at least one photoelectrode, wired photovoltaic(s), and a wired catalyst. Semiconductor/PV materials are shown in black, catalysts are in red, and protecting/contact layers are in blue

(Photo)cathode	(Photo)anode	Photovoltaic	Initial STH (%)	Stability (h)	Average J (mA cm^{-2})	Charge Passed (C)	H_2 Produced (mL cm^{-2})	First Author	Year	Ref #
Pt	(FeOOH/NiOOH)/$BiVO_4$	OPV	2.2	1	1.7	6.1	0.7	Peng	2017	81
Pt/Ti/Si	DSA	Perovskite	17.6	0.11	14	5.6	0.6	Karuturi	2020	82
NiMo	$FeNiO_x$/Al_2O_3/Fe_2O_3	Perovskite	1.9	0.83	1.5	4.4	0.5	Morales-Guio	2015	83
Pt	Ru(bda)L_2/DSSC	OPV	1.5	1	1	3.6	0.4	Wang	2020	84
Pt/Ti	WO_3	DSSC	1.9[1]	0.5	1.6	2.8	0.3	Park	2006	85
Pt	CoO_x/$BiVO_4$/WO_3/SnO_2	Perovskite	3.5	0.17[2]	3	1.8	0.2	Baek	2016	86
Pt/TiO_2/AZO/CdS/CIGS	DSA	Perovskite	6.3	0.025[3]	5.0	0.5	0.1	Luo	2015	87
Pt	CoPi/$BiVO_4$	Perovskite	2.5	0.042[4]	1.5	0.2	0.03	Chen	2015	88
Pt	CoPi/SnO_x:Fe_2O_3	Perovskite	3.4	0.017[5]	2.5	0.2	0.02	Gurudayal	2017	89
Pt/Ti/TiO_2/HIT-Si	IrO_x	HIT-Si/HIT-Si	12.2	--				Tan	2019	90
Pt	CoPi/Fe_2O_3	DSSC/DSSC	1.36	--				Brillet	2009	91

[1] 2-sun illumination
[2] chopped illumination for 15 min (10 min illuminated)
[3] chopped illumination for 3 min (1.5 min illuminated)
[4] chopped illumination for 5 min (2.5 min illuminated)

Supplemental References

(1) Geisz, J. F.; Levander, A. X.; Norman, A. G.; Jones, K. M.; Romero, M. J. *In Situ* Stress Measurement for MOVPE Growth of High Efficiency Lattice-Mismatched Solar Cells. *J. Cryst. Growth* **2008**, *310*, 2339–2344, DOI: 10.1016/j.jcrysgro.2007.11.048.

(2) Jain, N.; Geisz, J. F.; France, R. M.; Norman, A. G.; Steiner, M. A. Enhanced Current Collection in 1.7 EV GaInAsP Solar Cells Grown on GaAs by Metalorganic Vapor Phase Epitaxy. *IEEE J. Photovoltaics* **2017**, *7*, 927–933, DOI: 10.1109/JPHOTOV.2017.2655035.

(3) Jain, N.; Schulte, K. L.; Geisz, J. F.; Friedman, D. J.; France, R. M.; Perl, E. E.; Norman, A. G.; Guthrey, H. L.; Steiner, M. A. High-Efficiency Inverted Metamorphic 1.7/1.1 EV GaInAsP/GaInAs Dual-Junction Solar Cells. *Appl. Phys. Lett.* **2018**, *112*, 053905, DOI: 10.1063/1.5008517.

(4) Britto, R. J.; Benck, J. D.; Young, J. L.; Hahn, C.; Deutsch, T. G.; Jaramillo, T. F. Molybdenum Disulfide as a Protection Layer and Catalyst for Gallium Indium Phosphide Solar Water Splitting Photocathodes. *J. Phys. Chem. Lett.* **2016**, *7*, 2044–2049, DOI: 10.1021/acs.jpclett.6b00563.

(5) Young, J. L.; Steiner, M. A.; Döscher, H.; France, R. M.; Turner, J. A.; Deutsch, T. G. Direct Solar-to-Hydrogen Conversion via Inverted Metamorphic Multi-Junction Semiconductor Architectures. *Nat. Energy* **2017**, *2*, 17028, DOI: 10.1038/nenergy.2017.28.

(6) Deutsch, T. G.; Koval, C. A.; Turner, J. A. III−V Nitride Epilayers for Photoelectrochemical Water Splitting: GaPN and GaAsPN. *J. Phys. Chem. B* **2006**, *110*, 25297–25307, DOI: 10.1021/jp0652805.

(7) ASTM International. *ASTM G173-03(2012) Standard Tables for Reference Solar Spectral Irradiances: Direct Normal and Hemispherical on 37° Tilted Surface*; West Conshohocken, PA, 2012.

(8) Döscher, H.; Young, J. L.; Geisz, J. F.; Turner, J. A.; Deutsch, T. G. Solar-to-Hydrogen Efficiency: Shining Light on Photoelectrochemical Device Performance. *Energy Environ. Sci.* **2016**, *9*, 74–80, DOI: 10.1039/C5EE03206G.

(9) Chen, Z.; Jaramillo, T. F.; Deutsch, T. G.; Kleiman-Shwarsctein, A.; Forman, A. J.; Gaillard, N.; Garland, R.; Takanabe, K.; Heske, C.; Sunkara, M.; McFarland, E. W.; Domen, K.; Milled, E. L.; Dinh, H. N. Accelerating Materials Development for Photoelectrochemical Hydrogen Production: Standards for Methods, Definitions, and Reporting Protocols. *J. Mater. Res.* **2010**, *25*, 3–16, DOI: 10.1557/jmr.2010.0020.

(10) Benck, J. D.; Lee, S. C.; Fong, K. D.; Kibsgaard, J.; Sinclair, R.; Jaramillo, T. F. Designing Active and Stable Silicon Photocathodes for Solar Hydrogen Production Using Molybdenum Sulfide Nanomaterials. *Adv. Energy Mater.* **2014**, *4*, 1400739, DOI: 10.1002/aenm.201400739.

(11) Khaselev, O.; Turner, J. A. Electrochemical Stability of P-$GaInP_2$ in Aqueous Electrolytes Toward Photoelectrochemical Water Splitting. *J. Electrochem. Soc.* **1998**, *145*, 3335–3339, DOI: 10.1149/1.1838808.

(12) Moon, R. L.; Antypas, G. A.; James, L. W. Bandgap and Lattice Constant of GaInAsP as a Function of Alloy Composition. *J. Electron. Mater.* **1974**, *3*, 635–644, DOI: 10.1007/BF02655291.

(13) Haussener, S.; Hu, S.; Xiang, C.; Weber, A. Z.; Lewis, N. S. Simulations of the Irradiation and Temperature Dependence of the Efficiency of Tandem Photoelectrochemical Water-

Splitting Systems. *Energy Environ. Sci.* **2013**, *6*, 3605–3618, DOI: 10.1039/c3ee41302k.

(14) Welter, K.; Smirnov, V.; Becker, J. P.; Borowski, P.; Hoch, S.; Maljusch, A.; Jaegermann, W.; Finger, F. The Influence of Operation Temperature and Variations of the Illumination on the Performance of Integrated Photoelectrochemical Water-Splitting Devices. *ChemElectroChem* **2017**, *4*, 2099–2108, DOI: 10.1002/celc.201700112.

(15) Ding, C.; Qin, W.; Wang, N.; Liu, G.; Wang, Z.; Yan, P.; Shi, J.; Li, C. Solar-to-Hydrogen Efficiency Exceeding 2.5% Achieved for Overall Water Splitting with an All Earth-Abundant Dual-Photoelectrode. *Phys. Chem. Chem. Phys.* **2014**, *16*, 15608–15614, DOI: 10.1039/c4cp02391a.

(16) Hayashi, T.; Niishiro, R.; Ishihara, H.; Yamaguchi, M.; Jia, Q.; Kuang, Y.; Higashi, T.; Iwase, A.; Minegishi, T.; Yamada, T.; Domen, K.; Kudo, A. Powder-Based $(CuGa_{1-y}In_y)_{1-x}Zn_{2x}S_2$ Solid Solution Photocathodes with a Largely Positive Onset Potential for Solar Water Splitting. *Sustain. Energy Fuels* **2018**, *2*, 2016–2024, DOI: 10.1039/C8SE00079D.

(17) Kobayashi, H.; Sato, N.; Orita, M.; Kuang, Y.; Kaneko, H.; Minegishi, T.; Yamada, T.; Domen, K. Development of Highly Efficient $CuIn_{0.5}Ga_{0.5}Se_2$-Based Photocathode and Application to Overall Solar Driven Water Splitting. *Energy Environ. Sci.* **2018**, *11*, 3003–3009, DOI: 10.1039/c8ee01783b.

(18) May, M. M.; Lewerenz, H.-J.; Lackner, D.; Dimroth, F.; Hannappel, T. Efficient Direct Solar-to-Hydrogen Conversion by in Situ Interface Transformation of a Tandem Structure. *Nat. Commun.* **2015**, *6*, 8286, DOI: 10.1038/ncomms9286.

(19) Chen, M.; Liu, Y.; Li, C.; Li, A.; Chang, X.; Liu, W.; Sun, Y.; Wang, T.; Gong, J. Spatial Control of Cocatalysts and Elimination of Interfacial Defects towards Efficient and

Robust CIGS Photocathodes for Solar Water Splitting. *Energy Environ. Sci.* **2018**, *11*, 2025–2034, DOI: 10.1039/c7ee03650g.

(20) Martinez-Garcia, A.; Russell, H. B.; Paxton, W.; Ravipati, S.; Calero-Barney, S.; Menon, M.; Richter, E.; Young, J.; Deutsch, T.; Sunkara, M. K. Unassisted Water Splitting Using a $GaSb_xP_{(1-x)}$ Photoanode. *Adv. Energy Mater.* **2018**, *8*, 1703247, DOI: 10.1002/aenm.201703247.

(21) Wang, X.; Peng, K. Q.; Hu, Y.; Zhang, F. Q.; Hu, B.; Li, L.; Wang, M.; Meng, X. M.; Lee, S. T. Silicon/Hematite Core/Shell Nanowire Array Decorated with Gold Nanoparticles for Unbiased Solar Water Oxidation. *Nano Lett.* **2014**, *14*, 18–23, DOI: 10.1021/nl402205f.

(22) Kang, D.; Young, J. L.; Lim, H.; Klein, W. E.; Chen, H.; Xi, Y.; Gai, B.; Deutsch, T. G.; Yoon, J. Printed Assemblies of GaAs Photoelectrodes with Decoupled Optical and Reactive Interfaces for Unassisted Solar Water Splitting. *Nat. Energy* **2017**, *2*, 17043, DOI: 10.1038/nenergy.2017.43.

(23) Sakai, Y.; Sugahara, S.; Matsumura, M.; Nakato, Y.; Tsubomura, H. Photoelectrochemical Water Splitting by Tandem Type and Heterojunction Amorphous Silicon Electrodes. *Can. J. Chem.* **1988**, *66*, 1853–1856, DOI: 10.1139/v88-299.

(24) Peng, Y.; Govindaraju, G. V.; Lee, D. K.; Choi, K. S.; Andrew, T. L. Integrating a Semitransparent, Fullerene-Free Organic Solar Cell in Tandem with a $BiVO_4$ Photoanode for Unassisted Solar Water Splitting. *ACS Appl. Mater. Interfaces* **2017**, *9*, 22449–22455, DOI: 10.1021/acsami.7b04486.

(25) Karuturi, S. K.; Shen, H.; Sharma, A.; Beck, F. J.; Varadhan, P.; Duong, T.; Narangari, P. R.; Zhang, D.; Wan, Y.; He, J.; Tan, H. H.; Jagadish, C.; Catchpole, K. Over 17%

Efficiency Stand-Alone Solar Water Splitting Enabled by Perovskite-Silicon Tandem Absorbers. *Adv. Energy Mater.* **2020**, *2000772*, 2000772, DOI: 10.1002/aenm.202000772.

(26) Morales-Guio, C. G.; Mayer, M. T.; Yella, A.; Tilley, S. D.; Grätzel, M.; Hu, X. An Optically Transparent Iron Nickel Oxide Catalyst for Solar Water Splitting. *J. Am. Chem. Soc.* **2015**, *137*, 9927–9936, DOI: 10.1021/jacs.5b05544.

(27) Wang, D.; Hu, J.; Sherman, B. D.; Sheridan, M. V.; Yan, L.; Dares, C. J.; Zhu, Y.; Li, F.; Huang, Q.; You, W.; Meyer, T. J. A Molecular Tandem Cell for Efficient Solar Water Splitting. *Proc. Natl. Acad. Sci. U. S. A.* **2020**, *117*, 13256–13260, DOI: 10.1073/pnas.2001753117.

(28) Park, J. H.; Bard, A. J. Photoelectrochemical Tandem Cell with Bipolar Dye-Sensitized Electrodes for Vectorial Electron Transfer for Water Splitting. *Electrochem. Solid-State Lett.* **2006**, *9*, 6–9, DOI: 10.1149/1.2140497.

(29) Baek, J. H.; Kim, B. J.; Han, G. S.; Hwang, S. W.; Kim, D. R.; Cho, I. S.; Jung, H. S. $BiVO_4/WO_3/SnO_2$ Double-Heterojunction Photoanode with Enhanced Charge Separation and Visible-Transparency for Bias-Free Solar Water-Splitting with a Perovskite Solar Cell. *ACS Appl. Mater. Interfaces* **2017**, *9*, 1479–1487, DOI: 10.1021/acsami.6b12782.

(30) Luo, J.; Li, Z.; Nishiwaki, S.; Schreier, M.; Mayer, M. T.; Cendula, P.; Lee, Y. H.; Fu, K.; Cao, A.; Nazeeruddin, M. K.; Romanyuk, Y. E.; Buecheler, S.; Tilley, S. D.; Wong, L. H.; Tiwari, A. N.; Grätzel, M. Targeting Ideal Dual-Absorber Tandem Water Splitting Using Perovskite Photovoltaics and $CuIn_xGa_{1-x}Se_2$ Photocathodes. *Adv. Energy Mater.* **2015**, *5*, 1501520, DOI: 10.1002/aenm.201501520.

(31) Chen, Y. S.; Manser, J. S.; Kamat, P. V. All Solution-Processed Lead Halide Perovskite-$BiVO_4$ Tandem Assembly for Photolytic Solar Fuels Production. *J. Am. Chem. Soc.* **2015**,

137, 974–981, DOI: 10.1021/ja511739y.

(32) Gurudayal; John, R. A.; Boix, P. P.; Yi, C.; Shi, C.; Scott, M. C.; Veldhuis, S. A.; Minor, A. M.; Zakeeruddin, S. M.; Wong, L. H.; Grätzel, M.; Mathews, N. Atomically Altered Hematite for Highly Efficient Perovskite Tandem Water-Splitting Devices. *ChemSusChem* **2017**, *10*, 2449–2456, DOI: 10.1002/cssc.201700159.

(33) Tan, C. S. S.; Kemp, K. W.; Braun, M.; Meng, A. C.; Tan, W.; Chidsey, C. E. D.; Ma, W.; Moghadam, F.; Mc Intyre, P. C. >10% Solar-to-Hydrogen Efficiency Unassisted Water Splitting on ALD-Protected Silicon Heterojunction Solar Cells. *Sustain. Energy Fuels* **2019**, *3*, 1490–1500, DOI: 10.1039/c9se00110g.

(34) Brillet, J.; Comuz, M.; Formal, F. Le; Yum, J. H.; Grätzel, M.; Sivula, K. Examining Architectures of Photoanode-Photovoltaic Tandem Cells for Solar Water Splitting. *J. Mater. Res.* **2010**, *25*, 17–24, DOI: 10.1557/jmr.2010.0009.